A&A 638, A93 (2020)
https://doi.org/10.1051/0004-6361/202038117

Astronomy & Astrophysics

An in-depth reanalysis of the alleged type Ia supernova progenitor Henize 2−428

N. Reindl[1], V. Schaffenroth[1], M. M. Miller Bertolami[2,3], S. Geier[1], N. L. Finch[4], M. A. Barstow[4], S. L. Casewell[4], and S. Taubenberger[5]

[1] Institute for Physics and Astronomy, University of Potsdam, Karl-Liebknecht-Str. 24/25, 14476 Potsdam, Germany
e-mail: nreindl885@gmail.com
[2] Instituto de Astrofísica de La Plata, UNLP-CONICET, La Plata 1900, Buenos Aires, Argentina
[3] Facultad de Ciencias Astronómicas y Geofísicas, UNLP, Buenos Aires, Argentina Paseo del Bosque s/n, FWA, 1900 La Plata, Buenos Aires, Argentina
[4] Department of Physics and Astronomy, University of Leicester, University Road, Leicester LE1 7RH, UK
[5] Max Planck Institut für Astrophysik, Karl-Schwarzschild-Straße 1, 85748 Garching, Germany

Received 7 April 2020 / Accepted 14 May 2020

ABSTRACT

Context. The nucleus of the planetary nebula Hen 2-428 is a short orbital-period (4.2 h), double-lined spectroscopic binary, whose status as a potential supernova type Ia progenitor has raised some controversy in the literature.
Aims. With the aim of resolving this debate, we carried out an in-depth reanalysis of the system.
Methods. Our approach combines a refined wavelength calibration, thorough line-identifications, improved radial-velocity measurements, non-LTE spectral modeling, as well as multi-band light-curve fitting. Our results are then discussed in view of state-of-the-art stellar evolutionary models.
Results. Besides systematic zero-point shifts in the wavelength calibration of the OSIRIS spectra which were also used in the previous analysis of the system, we found that the spectra are contaminated with diffuse interstellar bands. Our Voigt-profile radial velocity fitting method, which considers the additional absorption of these diffuse interstellar bands, reveals significantly lower masses ($M_1 = 0.66 \pm 0.11\,M_\odot$ and $M_2 = 0.42 \pm 0.07\,M_\odot$) than previously reported and a mass ratio that is clearly below unity. Our spectral and light curve analyses lead to consistent results, however, we find higher effective temperatures and smaller radii than previously reported. Moreover, we find that the red-excess that was reported before to prove to be a mere artifact of an outdated reddening law that was applied.
Conclusions. Our work shows that blends of He II λ 5412 Å with diffuse interstellar bands have led to an overestimation of the previously reported dynamical masses of Hen 2−428. The merging event of Hen 2−428 will not be recognised as a supernova type Ia, but most likely leads to the formation of a H-deficient star. We suggest that the system was formed via a first stable mass transfer episode, followed by common envelope evolution, and it is now composed of a post-early asymptotic giant branch star and a reheated He-core white dwarf.

Key words. stars: individual: Hen 2−428 – binaries: spectroscopic – binaries: close – ISM: lines and bands

1. Introduction

The detection and analysis of compact binary systems is fundamental to various areas of astrophysics (Jones 2020). Binary interactions are thought to play a key role in the shaping of planetary nebulae (PNe, De Marco et al. 2009; Jones 2019) and are needed to explain the formation of diverse objects, such as hot sub-dwarf stars, extremely low mass white dwarfs (Paczynski 1976; Webbink 1984; Iben & Tutukov 1986), or post-red giant branch (RGB) central stars of planetary nebulae (CSPNe, Hall et al. 2013; Hillwig et al. 2017). Compact binaries are crucial to understand common envelope (CE) evolution and they serve as important tests for general relativity as very close binary systems (periods of less than a few hours) emit considerable amounts of gravitational radiation (Weisberg & Taylor 2005; Burdge et al. 2019).

The emission of gravitational waves in very close white dwarf binary systems leads to a shrinkage of their orbits resulting in mass transfer between the white dwarfs or even the merger of the white dwarfs. The ultimate fate of these systems depends on their total mass as well as the mass ratio, $q = M_2/M_1$, and whether mass transfer remains dynamically stable or not (Shen 2015). The outcomes of such interaction have been proposed to lead to the formation of exotic objects showing He-dominated atmospheres such as R Coronae Borealis stars (RCB), extreme helium (EHe) stars, He-rich hot subdwarf O (He-sdO) stars, or O(He) stars (Webbink 1984; Iben & Tutukov 1984; Saio & Jeffery 2002; Justham et al. 2011; Zhang & Jeffery 2012a,b; Zhang et al. 2014; Reindl et al. 2014a). Also stars with C/O-dominated atmospheres such as the very hot white dwarfs H1504+65 and RXJ0439.8−6809 (Werner & Rauch 2015), WO-type central stars (Gvaramadze et al. 2019), or hot DQ white dwarfs (Kawka et al. 2020) have been proposed to be the outcome of such mergers.

For sufficiently high mass progenitors the merger of the two white dwarfs can also lead to Type Ia supernovae (SN Ia) or faint thermonuclear supernovae (SN .Ia), which reach only one-tenth of the brightness of a SN Ia. This may occur via the so-called double-degenerate channel in which the resulting merger has a mass near the Chandrasekhar limit (Iben & Tutukov 1984; Webbink 1984), but various other evolutionary pathways for the double degenerate SN Ia channel have

been proposed for which the progenitor systems may also have sub-Chandrasekhar masses. These include the double-detonation mechanism (Woosley & Weaver 1994; Fink et al. 2007, 2010; Liu et al. 2018; Shen et al. 2018), the violent merger model (Pakmor et al. 2011, 2013; Liu et al. 2016), or the core degenerate channel (Sparks & Stecher 1974; Kashi & Soker 2011).

The detection of progenitor systems for the double-degenerate SN Ia model is extremely challenging as recently demonstrated by Rebassa-Mansergas et al. (2019), who predict an observational probability only of the order 10^{-5} for finding double white dwarf SN Ia progenitors in our Galaxy with current telescopes. Large observational efforts to search for double-degenerate SN Ia progenitor systems amongst double white dwarfs or white dwarf and pre-white dwarf (hot subdwarf) systems (Napiwotzki et al. 2001, 2020; Geier et al. 2011; Breedt et al. 2017) have revealed some progenitor candidates (Maoz et al. 2014), but none of them has been confirmed unambiguously and robustly. The only exception might be the binary system residing in the planetary nebula Hen 2−428, which is subject of this paper.

Hen 2−428 was discovered by Henize (1976) and a first hint of the binarity of its nucleus was suggested by Rodríguez et al. (2001) based on the discovery of a red-excess emission. The non-ambiguous evidence that Hen 2−428 hosts a binary central star, was only delivered by Santander-García et al. (2015, hereafter SG+15). They made the stunning discovery that the system is a double-lined spectroscopic binary system composed of two hot pre-white dwarfs. Fitting Gaussian profiles to the double lined and time variable He II λ 5412 Å line they found the radial velocity (RV) semi-amplitudes of both stars to be the same ($206 \pm 8\,\mathrm{km\,s^{-1}}$ and $206 \pm 12\,\mathrm{km\,s^{-1}}$). In addition, they derived a photometric period of 4.2 h and showed that the light curves can be reproduced assuming an over-contact system seen at an inclination angle of $i = 64.7 \pm 1.4°$. From this they derived dynamical masses of $0.88 \pm 0.13\,M_\odot$ for both stars, and concluded that the system is composed of two hot pre-white dwarfs with a combined mass higher than the Chandrasekar limit which will merge within 700 million years triggering a SN Ia.

This scenario has since been challenged by García-Berro et al. (2016), who criticized the strong mismatch between the luminosities and radii of both pre-white dwarf components as derived by SG+15 with the predictions from single-star stellar evolution models (Bloecker & Schoenberner 1991; Bloecker 1993; Renedo et al. 2010). In addition, García-Berro et al. (2016) suggested that the variable He II λ 5412 Å line might instead be a superposition of an absorption line plus an emission line, possibly arising from the nebula, the irradiated photosphere of a close companion, or a stellar wind. Since this would question the dynamical masses derived by SG+15, García-Berro et al. (2016) repeated the light curve fitting and showed that the light curves of Hen 2−428 may also be fitted well by assuming an over-contact binary system that consists of two lower mass (i.e., masses of $0.47\,M_\odot$ and $0.48\,M_\odot$) stars. Thus, they concluded that the claim that Hen 2−428 provides observational evidence for the double degenerate scenario for SN Ia is premature.

Given the potential importance of Hen 2−428 as a unique laboratory to study the double degenerate merger scenario, it is highly desirable to resolve this debate. This is the goal of this work. The paper is organized as follows. In Sect. 2, we give an overview of the available observations, and provide a detailed description of continuum and line contributions to the spectra (Sect. 2.2). In Sect. 3, we examine the wavelength calibration accuracy and perform an improved RV analysis. After that we carry out a non-LTE spectral analysis to derive atmospheric parameters (Sect. 4) and perform multi-band light-curve fits (Sect. 5). The dynamical masses are presented in Sect. 6 along with a discussion of the evolutionary status of the system. We summarize and present our conclusions in Sect. 7.

2. Observations

2.1. Photometry

SG+15 obtained time-resolved *i*-band (effective wavelength 0.44 μm) photometry with the MERcator Optical Photometric ImagEr (MEROPE, Davignon et al. 2004) on the *Mercator* telescope on La Palma on 28 and 30 August 2009, and on 2 September 2009. Another *i*-band time-series was obtained by them on 2 August 2013 with the Wide Field Camera at the 2.5m *Isaac Newton* Telescope (INT) as well as a Johnson *B*-band (effective wavelength 0.78 μm) time-series with the South African Astronomical Observatory (SAAO) 1 m telescope on 11 July 2013. In addition, we acquired Asteroid Terrestrial-impact Last Alert System (ATLAS, Tonry et al. 2018) *c*- and *o*-band light curves (effective wavelengths 0.53 μm and 0.68 μm, respectively) of Hen 2−428.

2.2. Spectroscopy

Low-resolution spectroscopy of Hen 2−428 was obtained by Rodríguez et al. (2001) using the Intermediate Dispersion Spectrograph (IDS) at the INT. These observations have a spectral resolution of ≈8 Å and cover the wavelength range of 3500−9000 Å.

SG+15 obtained four observations with the FOcal Reducer/low dispersion Spectrograph 2 (FORS2) mounted on the Unit Telescope 1 (UT1) of the ESO Very Large Telescope (VLT) array (ProgIDs: 085.D-0629(A), 089.D-0453(A)). The observations were obtained in 2010 and 2012 using the 1200G grism (spectral resolution of ≈3 Å, resolving power $R = 1605$). We downloaded these observations from the ESO archive and reduced them using standard IRAF procedures.

The most useful set of observations (15 exposures in total, Table 1) was obtained at the Gran Telescopio Canarias (GTC) using the Optical System for Imaging and low Resolution Integrated Spectroscopy (OSIRIS) with the R2000B grating (ProgID: GTC41-13A). The spectra ($R = 2165$) with a mean exposure time of 868 s cover the full orbital period of the system and were used by SG+15 to derive the RV curves of the system. The signal-to-noise ratio (S/N) of these observations is similar to the ones of the FORS2 observations (≈70 at 4600 Å), but they have a higher resolution (2 Å instead of 3 Å). We downloaded the OSIRIS observations that were reduced by SG+15 from the GTC Public Archive.

Additionally, we obtained observations using the UV-Visual high-resolution Echelle Spectrograph (UVES) mounted at the 8.2 m Kueyen (UT2) telescope (ProgID: 295.D-5032(A)). The poor signal to noise ($S/N \approx 5$) of these spectra, however, does not allow the identification of photospheric lines, thus we discarded these observations from our analysis of the central stars.

The spectra of Hen 2−428 are a complex superposition of nebular, photospheric, interstellar, and circumstellar contributions. The continuum flux is noticeably affected by interstellar and circumstellar reddening and – as claimed by Rodríguez et al. (2001) – possibly by a late type companion that causes a red-excess. For the further analysis it is crucial to first disentangle and check these various contributions.

Table 1. OSIRIS observations of Hen 2−428.

Nr.	ID	HJD_{middle}	t_{exp} [s]	Hδ [km s^{-1}]	Hγ [km s^{-1}]	Hβ [km s^{-1}]	Hδ,γ,β [km s^{-1}]
#1	0000411146	2456516.44874	868	65 ± 3	65 ± 1	69 ± 1	66 ± 1
#2	0000411147	2456516.45964	868	67 ± 5	67 ± 2	69 ± 2	68 ± 6
#3	0000411148	2456516.47053	868	62 ± 6	62 ± 2	65 ± 1	63 ± 2
#4	0000411149	2456516.48142	868	56 ± 2	55 ± 2	59 ± 2	56 ± 4
#5	0000411150	2456516.49231	868	53 ± 3	54 ± 1	58 ± 2	55 ± 5
#6	0000411152	2456516.52202	650	34 ± 2	35 ± 1	42 ± 2	37 ± 5
#7	0000411161	2456516.55371	868	30 ± 3	33 ± 1	39 ± 4	34 ± 4
#8	0000411162	2456516.56460	868	28 ± 2	28 ± 2	35 ± 2	30 ± 2
#9	0000411163	2456516.57549	868	29 ± 3	28 ± 3	36 ± 2	31 ± 5
#10	0000411164	2456516.58638	868	17 ± 2	17 ± 3	23 ± 2	19 ± 6
#11	0000411165	2456516.59728	868	14 ± 3	14 ± 3	20 ± 2	16 ± 5
#12	0000411166	2456516.60817	868	12 ± 3	11 ± 4	20 ± 4	14 ± 6
#13	0000411167	2456516.61906	868	20 ± 2	17 ± 3	21 ± 2	19 ± 4
#14	0000411168	2456516.62995	868	20 ± 3	16 ± 2	20 ± 1	19 ± 5
#15	0000411169	2456516.64084	868	24 ± 3	20 ± 2	22 ± 3	22 ± 5

Notes. The Heliocentric Julian Day at middle of the exposure, exposure times, and RVs as measured from the different Balmer lines (indicating the drift of the zero-point in course of the observing run) are listed.

2.2.1. Nebular contributions

The nebula only contributes a negligible fraction to the continuum flux, for instance Rodríguez et al. (2001) estimated that the strongest source of nebular continuum (the recombination continuum of H I) may only account for a few percent to the total flux in the optical. Much more prominent are the nebular emission lines, which are labeled in black in Fig. 1 where we show the coadded OSIRIS spectrum.

For the nebular line identifications we made use of the nebular line list for Hen 2−428 provided in Rodríguez et al. (2001), published line lists of other PNe (Zhang et al. 2012; Corradi et al. 2015), as well as The Atomic Line List v2.05b21[1] (van Hoof 2018). Thanks to the higher resolution of the OSIRIS spectra compared to the IDS spectra used in the nebular analysis by Rodríguez et al. (2001), we found in addition also collisionally excited lines of [Cl III], [Ar I], [Ar IV], [Fe I], [Fe II], and [Fe III] as well as optical recombination lines of N III and O II. The latter could be blended with photospheric lines, but since they do not vary over the orbital period, we conclude that these lines mainly originate from the nebula.

With regard to the concept of García-Berro et al. (2016), that the small reversals in the cores of the He II lines might originate from nebular emission lines, we note that in this case the nebular line flux of He II λ 4686 Å should be about one order of magnitude higher than that of the remaining He II lines (e.g., Zhang et al. 2012). In addition, it was already reported by Tylenda et al. (1994) and SG+15 that Hen 2−428 does not show the He II λ 4686 Å nebular line. Therefore, the presence of the He II $\lambda\lambda$ 4200, 4542, 5412 Å nebular lines, which are much weaker, can be excluded as well. We also note that no He II emission lines can be detected in the UVES observations.

2.2.2. Photospheric contributions

The spectra show photospheric absorption lines of H I $\lambda\lambda$ 4102, 4340, 4861 Å which are blended with photospheric absorption lines of He II $\lambda\lambda$ 4100, 4339, 4859 Å, as well as He I $\lambda\lambda$ 4026, 4388, 4472, 4922 Å (marked in red in Fig. 1, He I $\lambda\lambda$ 4026 Å is blended with the weaker He II $\lambda\lambda$ 4026 Å). All of these lines are blended with nebular lines, i.e. they show photospheric absorption wings, while the line cores exhibit either H I or He I nebular emission lines. The only photospheric lines, which are not blended with nebular lines are He II $\lambda\lambda$ 4200, 4542, 4686, 5412 Å (marked in magenta in Fig. 1).

We also would like to comment here on the idea of García-Berro et al. (2016) that the He II λ 5412 Å line might be a superposition of a single absorption line plus an emission line. Compared to synthetic spectra for hot (pre-)white dwarfs, all He II lines in the spectra of Hen 2−428 are at the same time unusually broad and deep. This could, in principle, be explained by a pure He atmosphere of a very fast rotating star. However, then the observed absorption wings of the Balmer lines should be much weaker. Thus, we conclude that the He II lines are indeed double-lined and stem from the photospheres of the two hot stars as reported by SG+15. This is also perfectly supported by the RV analysis (Sect. 3).

The fluxes of the two hot stars constitute the dominant contribution to the continuum flux, whose shape is, however, altered by reddening which we will discuss in the next section.

2.2.3. Interstellar and circumstellar contributions

The determination of the reddening of the observations is important to investigate the nature of the claimed red-excess by Rodríguez et al. (2001), which could have a noticeable impact on the RV, light curve, and spectral analysis. This is because a cool companion might leave behind spectral features contaminating the spectrum and add an additional continuum light to both the spectroscopic and photometric observations. Furthermore, the knowledge of the reddening is also essential for the distance determination.

We determined the reddening by de-reddening the IDS and OSIRIS observations for different values of E_{B-V} with the reddening law of Fitzpatrick (1999) until a good agreement with our best fit model spectrum (see Sect. 4) was found. In Fig. 2, our best fit model is shown in red, the de-reddened OSIRIS spectrum #2 in gray, and the de-reddened IDS spectrum in black. For the IDS spectrum we find E_{B-V} = 1.15 ± 0.05 mag

[1] https://www.pa.uky.edu/~peter/newpage/

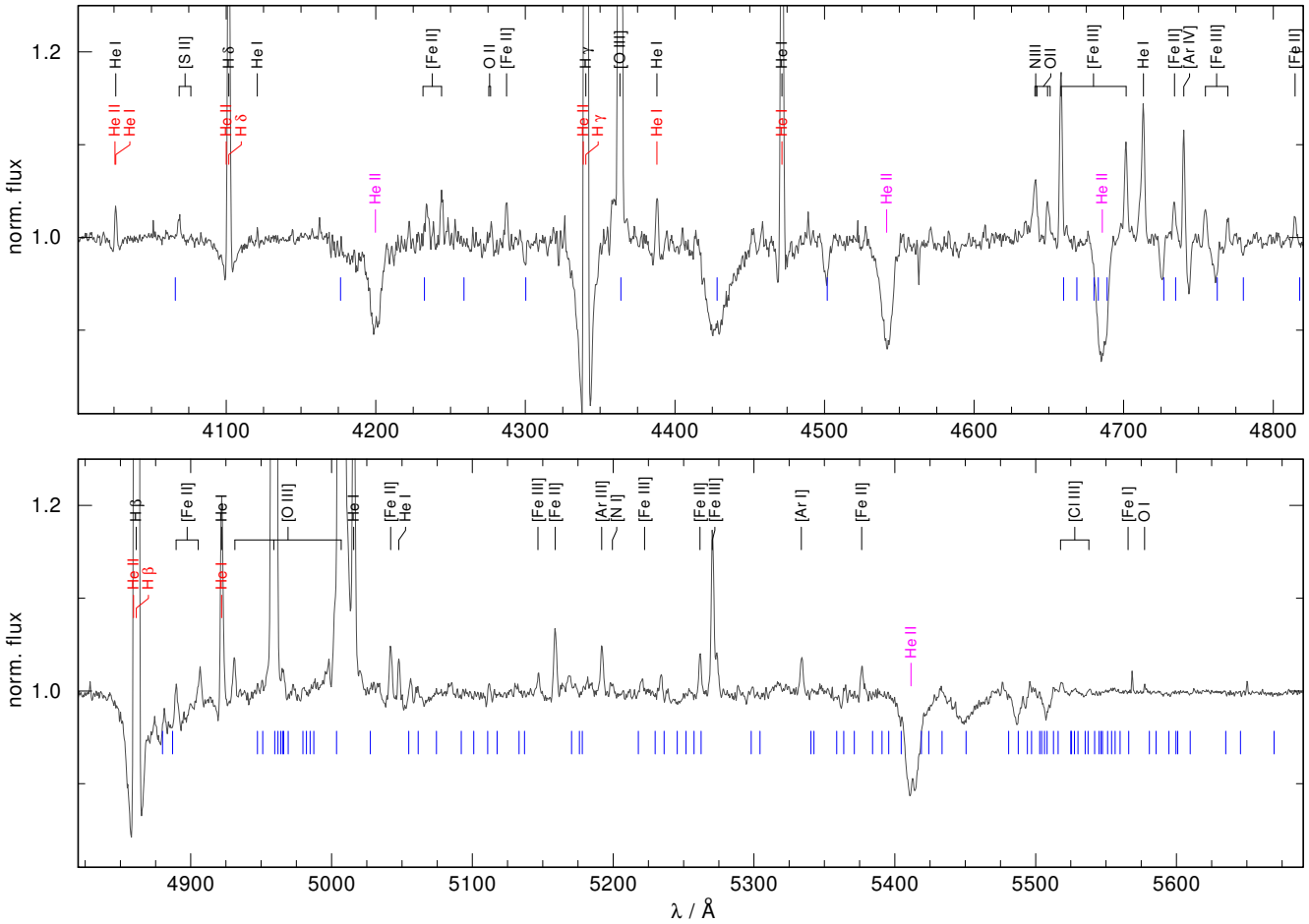

Fig. 1. Co-added and normalized OSIRIS spectrum. The locations of known diffuse interstellar bands (blue), nebular (black), and photospheric lines (red) are marked. Photospheric lines used in for the RV analysis are marked in magenta.

corresponding to $A_V = 3.57 \pm 0.16$ mag (assuming $R_V = 3.1$), while the OSIRS observations suggest a slightly higher value of $E_{B-V} = 1.20 \pm 0.05$ mag. Using the nebula line ratio of Hα/Hβ and the reddening law of Cardelli et al. (1989), Rodríguez et al. (2001) found $A_V = 2.96 \pm 0.34$ mag, which is about 20% smaller than the values derived by us[2].

In Fig. 2 we also show in blue the IDS spectrum de-reddened with the reddening law of Cardelli et al. (1989) instead of the Fitzpatrick (1999) law. This causes a clearly visible depression of the observed flux from 4400 to 5400 Å, which reaches its maximum deviation from the model spectrum around 4900 Å. The Cardelli reddening law is considered as outdated, i.e. based on fits to the location of the blue tip of the stellar locus in various SDSS fields, Schlafly et al. (2010) report that the Fitzpatrick reddening law is clearly favored over Cardelli. We therefore conclude that the red excess claimed by Rodríguez et al. (2001) is merely a consequence of the reddening law used, which makes it appear as if there is an increased continuum emission red-wards of about 5000 Å. This also implies that Hen 2−428 has likely no late-type companion, at least none that is noticeable in the optical wavelength range.

Hen 2−428 is located at a low galactic latitude ($b = 2.48°$) and embedded in the galactic disk, therefore the relatively high extinction towards this source is not surprising. The 3D Reddening Map of interstellar dust by Lallement et al. (2018)[3] extends to 2.63 kpc in the direction of Hen 2−428 (which is close to the distance given by Frew et al. (2016), who derived 2.72 ± 0.86 kpc using the Hα surface brightness–radius relation) and predictes $E_{B-V} = 0.81 \pm 0.05$. Thus, about one third of the reddening towards Hen 2−428 might be circumstellar and caused by the compact nebula.

Interstellar and circumstellar contributions, however, do not only leave a noticeable impact the continuum flux. The spectra of Hen 2−428 also exhibit numerous additional absorption lines, which we all identify as absorptions caused by diffuse interstellar bands (DIBs). These absorption features, often seen in highly reddened stars, originate in the interstellar medium (ISM) and are typically broader than expected from the Doppler broadening of turbulent gas motions in the ISM (Jenniskens & Desert 1994). DIBs are widely assumed to be caused by large molecules (e.g., C_{60}^+ Campbell et al. 2015), however, not all DIBs have yet been conclusively identified. In the wavelength range from 4000 to 10 000 Å, there are several classes of molecules considered to be possible DIB absorbers and which may produce a few strong bands along with a much larger array of weaker bands (Hobbs et al. 2008, and references therein).

The blue bars in Fig. 1 mark the locations of DIBs identified in the high-resolution, high S/N spectrum of HD 204827 by Hobbs et al. (2008). We note that due to the lower resolution and lower S/N of the OSIRIS observations, only

[2] We note that differences up to 50% in E_{B-V} as derived from different spectra or nebula lines have also been noticed in the CSPN SAO 245567 (Arkhipova et al. 2013; Reindl et al. 2014b).

[3] https://stilism.obspm.fr/

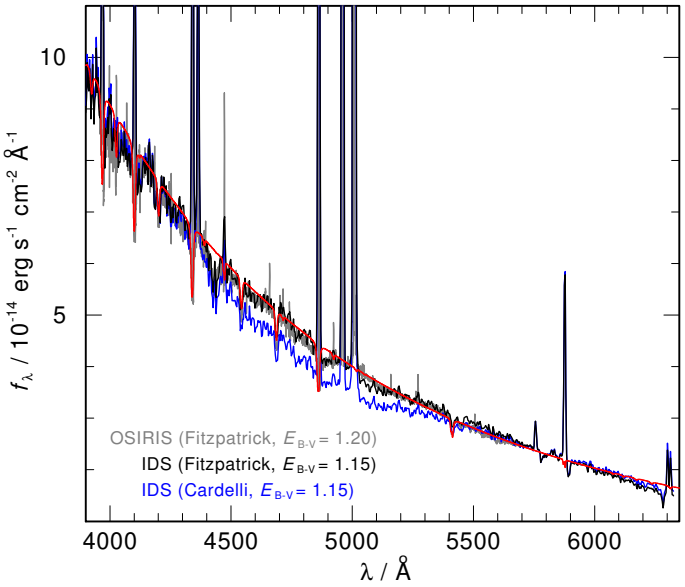

Fig. 2. Determination of the reddening. The OSIRIS spectrum #2 de-reddend with the Fitzpatrick reddening law (gray) and the IDS spectrum de-reddened once with the Fitzpatrick reddening law (black) and once with the Cardelli reddening law (blue) are compared to our best fit TMAP model (red).

relatively strong DIBs are visible. The strength of the most prominent DIB at 4430 Å resembles the strengths of the photospheric He II lines, but other strong DIBs at 4501.79, 4726.83, 4762.61, 5450.62, 5487.69, 5525.48 Å are clearly visible as well. HD 204827 has a very similar reddening (E_{B-V} = 1.11, Hobbs et al. 2008) compared to Hen 2−428 (E_{B-V} = 1.15, see above). Since the equivalent width of DIBs is correlated to the value of E_{B-V} (e.g., Kos & Zwitter 2013; Krełowski et al. 2019), one can expect that the DIBs in Hen 2−428 are of similar strengths to what is observed in HD 204827. A quite crucial point that now becomes obvious when looking at Fig. 1 is that three of the four He II lines are blended with DIBs. He II λ4686 Å and He II λ5412 Å are blended with three and four weaker DIBs, respectively. Bluewards (at about 4176 Å) of He II λ4200 Å a relatively broad and strong DIB is located, which was first noted by Jenniskens & Desert (1994) in the spectra of HD 30614, HD 21389, HD 190603, and HD 183143. This leaves only the He II λ4542 Å line unaffected by DIB absorption.

3. Radial velocity analysis

3.1. Wavelength calibration accuracy of the OSIRIS spectra

The accuracy of the wavelength calibration is a crucial point when determining the RVs of a binary system. We used the nebular lines to check the wavelength calibration of the OSIRIS spectra, as the RVs of these lines should not change over the orbital period and correspond to the system velocity. For that we first measured the RVs of the Balmer emission lines by fitting them with a set of mathematical functions (Gaussians, Lorentzians, and polynomials) using SPAS (Spectrum Plotting and Analysing Suite, Hirsch 2009). The error determination is done by using the bootstrapping method. We find that the line to line variations are small within a single exposure, suggesting an accuracy of the wavelength calibration of 5 km s^{-1} in the wavelength range 4101−4681 Å. However, the RVs of the Balmer lines from the different exposures show large variations, indicating zero-point shifts of the wavelength calibration up to 54 km s^{-1} (Table 1). Consequently, we corrected each observation for the RV measured by fitting all three Balmer emission lines simultaneously, which leaves us with an artifical system velocity of 0 km s^{-1}.

It is worth mentioning that wavelength calibration exposures for the OSIRIS spectra were taken only in the beginning of the observing run. Therefore, the velocity measured simultaneously from Hδ, Hγ, and Hβ from observation #1 (66 ± 1 km s^{-1}) should reflect the true system velocity. This value also agrees with the system velocity of 70 ± 8 km s^{-1} reported by Rodríguez et al. (2001).

To check the wavelength calibration in the red part of the spectra (i.e., around He II λ5412 Å, used by SG+15 to determine the masses), we measured the RVs of the Fe II λ5376 Å nebular line (closest nebular line to He II λ5412 Å) in the zero-point corrected observations. We found variations up to 68 km s^{-1} in the different spectra. Since those lines are relatively weak, we could not detect them in three of the fifteen observations and we also note that the average uncertainty on the measured RVs of Fe II λ5376 Å are 20 km s^{-1}. Therefore, we refrain from applying additional corrections to the spectra and merely state that the wavelength calibration accuracy seems to get worse than 5 km s^{-1} in the red part of the spectrum.

3.2. Radial velocity amplitudes

Since Gaussian line profiles as used by SG+15 only provide a good fit to the line cores of the He II lines but not to their wings, we used Voigt profiles to measure the RVs for both components. Using Python, Voigt profiles were calculated via the Faddeeva function and fitted to the zero-point corrected OSIRIS spectra using the non-linear least squares method of Levenberg-Marquardt (Jones et al. 2001). The semi-amplitudes of the RV curves (K_1, K_2) were then obtained by sinusoidal fitting of the individual RV measurements obtained for both components of the binary system. The system velocity, γ, the orbital period, P, and the zero point of the RV curve (the latter two within the uncertainties determined from the light curves by SG+15) were allowed to vary, but required to be the same for both stars.

Examples of the Voigt profile fits to the four observed He II lines (gray lines) are shown in Fig. 3, along with the resulting RV curves for each line. The red and blue lines correspond to the absorption lines and RV curves of the primary and secondary, respectively. The purple line indicates the combined fit. The black, dashed line in the RV curve plots indicates the system velocity (remember we applied an artifical system velocity of 0 km s^{-1} based on the H I nebular emission lines, see Sect. 3.1).

First, the RV fitting was performed assuming only two Voigt profiles for each He II feature corresponding to the absorption lines of the two stars. In case of He II λ4686 Å and He II λ5412 Å we next included additional, fixed Voigt profiles in order to simulate the DIBs (light blue, dashed lines in Fig. 3). The equivalent widths and full widths at half maximum of these DIBs were required to be the same as reported by Hobbs et al. (2008) for HD 204827. The DIB blue-ward of He II λ4200 Å, which also blends with this line, is clearly visible in the co-added OSIRIS spectrum (Fig. 3). Therefore, we obtained the Voigt profile for this DIB directly from the co-added OSIRIS spectrum, and used this line profile in each subsequent RV fit.

Neglecting DIBs, we find for He II λ5412 Å similar RV amplitudes of $K_1 = 178 \pm 17$ km s^{-1} and $K_2 = 209 \pm 18$ km s^{-1}, which is close to the values derived by SG+15 by Gaussian

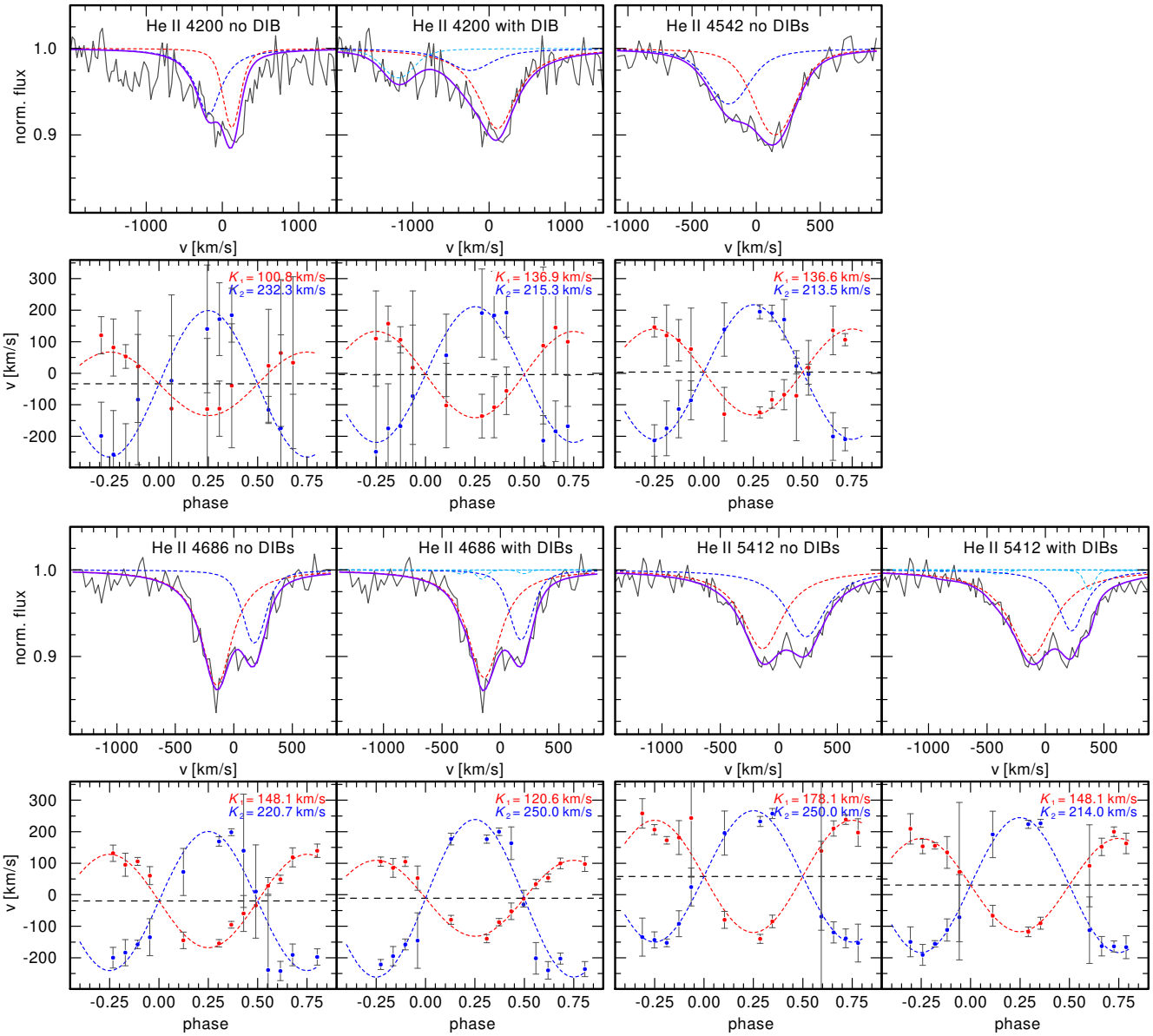

Fig. 3. Examples of Voigt profile fits (blue: secondary, red: primary, light blue: DIBs, purple: combined fit) to the four observed He II lines (gray). *Top panels*: observation #2 taken around phase −0.25, *bottom panels*: observation #7 taken around phase 0.28. RV curves (blue: secondary, red: primary) obtained for the respective He II lines with the RV amplitudes are shown below. The black, dashed line in RV curve plots indicates the system velocity.

fitting of the He II λ 5412 Å absorption lines ($K_1 = 206 \pm 8\,\mathrm{km\,s^{-1}}$ and $K_2 = 206 \pm 12\,\mathrm{km\,s^{-1}}$). We note that we obtain a system velocity much larger than zero ($\gamma = 58 \pm 9\,\mathrm{km\,s^{-1}}$), indicating already a problematic result. The picture, however, changes noticeably if additional DIB absorption lines are included in the RV fitting process. We then obtain very distinct RV amplitudes of $K_1 = 148 \pm 9\,\mathrm{km\,s^{-1}}$ and $K_2 = 214 \pm 10\,\mathrm{km\,s^{-1}}$, i.e. we find that the RV amplitude of the primary star could be $30\,\mathrm{km\,s^{-1}}$ smaller. The value for the system velocity ($\gamma = 31 \pm 5\,\mathrm{km\,s^{-1}}$) improves, but is still clearly larger than zero. This likely indicates that DIBs in Hen 2−428 are different to HD 204827 and/or that the wavelength calibration in the red part of the spectrum becomes slightly worse (see Sect. 3.1).

For He II λ 4686 Å we find two different RV amplitudes ($K_1 = 148 \pm 22\,\mathrm{km\,s^{-1}}$ and $K_2 = 221 \pm 24\,\mathrm{km\,s^{-1}}$) even if we neglect the DIBs. Including DIBs in the fitting, the differences become even more noticable ($K_1 = 121 \pm 18\,\mathrm{km\,s^{-1}}$ and $K_2 = 250 \pm 21\,\mathrm{km\,s^{-1}}$). Also in this case, the RV curve fitting suggests system velocities which are smaller than zero ($\gamma = -20 \pm 10\,\mathrm{km\,s^{-1}}$, when no DIBs are considered, and $\gamma = -11 \pm 9\,\mathrm{km\,s^{-1}}$, when the DIBs are included). However, the deviation from zero is not as drastic as in the case of He II λ 5412 Å.

An interesting point to notice is that the line profiles of He II λ 5412 Å of both the primary and secondary are very similar if DIBs are neglected. Including DIBs in the fits, the line of the secondary becomes much weaker (see the right hand panel in the second to last row of Fig. 3). For He II λ 4686 Å (which is blended with weaker DIBs than He II λ 5412 Å) and He II λ 4542 Å (not blended with any DIB) it is already evident from the observed line profiles, that the line of the secondary must be weaker than the line of the primary.

The RV amplitudes of He II λ 4542 Å are of greatest interest as it is the only line not blended with any DIB. For this line we obtain again very different RV amplitudes of

$K_1 = 137 \pm 12\,\mathrm{km\,s^{-1}}$ for the primary and $K_2 = 214 \pm 14\,\mathrm{km\,s^{-1}}$ for the secondary. This supports the results from the RV fits of He II λ4686 Å and He II λ5412 Å if DIBs are included. We also stress that in the case of He II λ4542 Å, we obtain a system velocity of only $4 \pm 6\,\mathrm{km\,s^{-1}}$, consistent with zero.

The blue parts of the OSIRIS spectra covering He II λ4200 Å have a lower S/N, resulting in larger uncertainties of the individual RV measurements. If we neglect the absorption of the broad DIB blue-ward of He II λ4200 Å, we obtain RV amplitudes of $K_1 = 101 \pm 25\,\mathrm{km\,s^{-1}}$ and $K_2 = 232 \pm 34\,\mathrm{km\,s^{-1}}$, and $\gamma = -34 \pm 10\,\mathrm{km\,s^{-1}}$. If we, however, include our DIB model which we obtained directly from the co-added spectrum (see above), we end up with RV amplitudes of $K_1 = 137 \pm 18\,\mathrm{km\,s^{-1}}$ and $K_2 = 215 \pm 21\,\mathrm{km\,s^{-1}}$, confirming the results from He II λ4542 Å surprisingly well. Also in this case we find that the system velocity is very small ($-4 \pm 9\,\mathrm{km\,s^{-1}}$) and consistent with zero.

In summary, if DIBs are not included in the RV fitting, we end up with conflicting RV semi-amplitudes for the four He II lines. However, when including the DIBs we obtain consistent results. Since our DIB models for He II λ4686 Å and He II λ5412 Å may not be perfect assumptions (as indicated from the non-zero system velocities), the RV amplitudes derived from He II λ4200 Å and He II λ4542 Å should be the ones to rely on. For these lines very distinct RV amplitudes are found as opposed to the findings of SG+15.

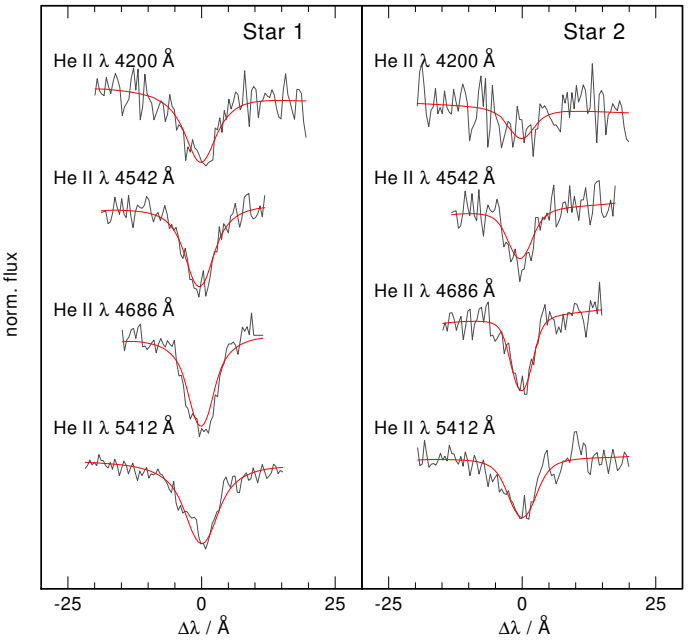

Fig. 4. He II lines of the decomposed OSIRIS spectrum #2 (gray) shown along with the best the fit TMAP models (red).

4. Atmospheric analysis

For the spectral analysis we restricted ourselves to the OSIRIS observation #2. This is because this observation was taken closest to maximum RV separation and, hence, smearing of the lines due to the orbital motion (i.e., the change of the RV over the duration of the exposure) is only a few $\mathrm{km\,s^{-1}}$ (close to phase 0 and 0.5 the orbital smearing reaches about $78\,\mathrm{km\,s^{-1}}$). Also in observations #2 none of the four He II lines are contaminated with emission lines. The spectrum was decomposed by subtracting the line profiles obtained from the RV fitting (Sect. 3) for the DIBs and the other star from the observation.

For the model calculations we employed the Tübingen non-LTE model-atmosphere package (TMAP[4], Werner et al. 2003, 2012; Rauch & Deetjen 2003) which allows plane-parallel, non-LTE, fully metal-line blanketed model atmospheres in radiative and hydrostatic equilibrium to be computed. Model atoms were taken from the Tübingen model atom database TMAD[5]. Metal-free model grids were calculated for six different He abundances ($\log \mathrm{He/H} = +2, +1, 0, -1, -2$, and -3, logarithmic number ratios). Each grid spans from $T_\mathrm{eff} = 30\,000$–$70\,000$ K (step size 2500 K) and from $\log g = 3.75$–6.0 (step size 0.25 dex). Models above the Eddington limit (i.e., $T_\mathrm{eff} > 60\,000$ K for $\log g = 4.25$, $T_\mathrm{eff} > 50\,000$ K for $\log g = 4.00$, and $T_\mathrm{eff} > 47\,500$ K for $\log g = 3.75$) were not calculated. To calculate synthetic line profiles, we used Stark line-broadening tables provided by Barnard et al. (1969) for He I $\lambda\lambda$4026, 4388, 4471, 4921 Å, Barnard et al. (1974) for He I λ4471 Å, and Griem (1974) for all other He I lines. For He II, we used the tables provided by Schöning & Butler (1989), and for H I tables provided by Tremblay & Bergeron (2009). For He II 20 levels were considered in non-LTE, for He I 29 levels, and for H I 15 levels.

To derive effective temperatures, surface gravities, and He abundances we fitted simultaneously all four decomposed He II lines of each star. The parameter fit was performed by means of a χ^2 minimization technique with SPAS (Spectrum Plotting and Analysing Suite, Hirsch 2009), which is based on the FITSB2 routine (Napiwotzki 1999). Although we do not expect the system to be fully synchronized shortly after a common envelope event, both stars have likely high rotational velocities. Therefore, we considered the projected rotational velocity $v \sin i$ as a forth parameter in our fit.

Our initial fit assumes a flux ratio of one, and the effective temperatures, surface gravities, He abundances, and rotational velocities were considered as free parameters. Based on these results we performed light curve fits (Sect. 5) and used the updated flux ratios and rotational velocities (assuming a synchronized system) to repeat the spectral fits. This iterative process was repeated until a good agreement between the results from the light curve fitting and the spectral analysis was obtained. In our final spectroscopic fit we assume a flux ratio of 1.4 and projected rotational velocities of $v \sin i = 156\,\mathrm{km\,s^{-1}}$ for the primary and $v \sin i = 133\,\mathrm{km\,s^{-1}}$ for the secondary.

Our best fits to spectrum #2 are shown in Fig. 4 and the results of our analysis are summarized in Table 2. We note that our best fit also reproduces very well the wings of the Balmer and He I lines (Fig. A.1). The effective temperatures ($T_\mathrm{eff} = 39\,555$ K and $T_\mathrm{eff} = 40\,858$ K, for the primary and secondary, respectively) and surface gravities ($\log g = 4.50$ and $\log g = 4.62$) obtained for both stars are found to be very similar and agree well within the error limits with the results from the light curve fitting (see Sect. 5 and Table 2). The He abundance of the primary ($X_\mathrm{He} = -0.16 \pm 0.10$, logarithmic mass fraction), which has the stronger lines, is found to be super solar ($X_{\mathrm{He}_\odot} = -0.60$, Asplund et al. 2009), while the secondary has a slightly sub-solar He abundance ($X_\mathrm{He} = -1.01 \pm 0.20$).

Our effective temperatures are larger than the ones reported by SG+15, who derived the effective temperatures from light curve fitting. The narrow temperature range (30–40 kK) adopted by SG+15, however, is not valid as already pointed out by García-Berro et al. (2016). SG+15 established the upper limit of 40 kK based on the absence of He II emission lines, but there are many CSPNe with even higher T_eff and which also lack

[4] http://astro.uni-tuebingen.de/~TMAP
[5] http://astro.uni-tuebingen.de/~TMAD

Table 2. Orbital and stellar parameters of Hen 2−428. He abundances are given in logarithmic mass fractions.

	Primary	Secondary
P [days] [(a)]	0.1758 ± 0.0005	
γ [km s^{-1}]	66 ± 1	
$q \equiv M_2/M_1$	$0.64^{+0.25}_{-0.18}$	
i [°]	63.59 ± 0.54	
a [$R_\odot$]	1.35 ± 0.07	
$T_{\rm eff}$ [K] (Spec.)	39555 ± 3000	40858 ± 4500
$T_{\rm eff}$ [K] (LC)	40179 ± 370	40356 ± 175
$\log g$ (Spec.)	4.50 ± 0.30	4.62 ± 0.30
$\log g$ (LC)	4.69 ± 0.03	4.64 ± 0.04
$X_{\rm He}$	-0.16 ± 0.10	-1.01 ± 0.20
$v_{\rm rot}$ [km s^{-1}] [(b)]	174	148
K_{4542} [km s^{-1}]	136.6 ± 12.0	213.5 ± 13.7
M_{4542} [$M_\odot$]	0.66 ± 0.11	0.42 ± 0.07
R [mean, $R_\odot$]	0.603 ± 0.038	0.514 ± 0.033
L [$L_\odot$]	803 ± 264	665 ± 305

Notes. [(a)]Taken from SG+15. [(b)]Assuming a synchronized system.

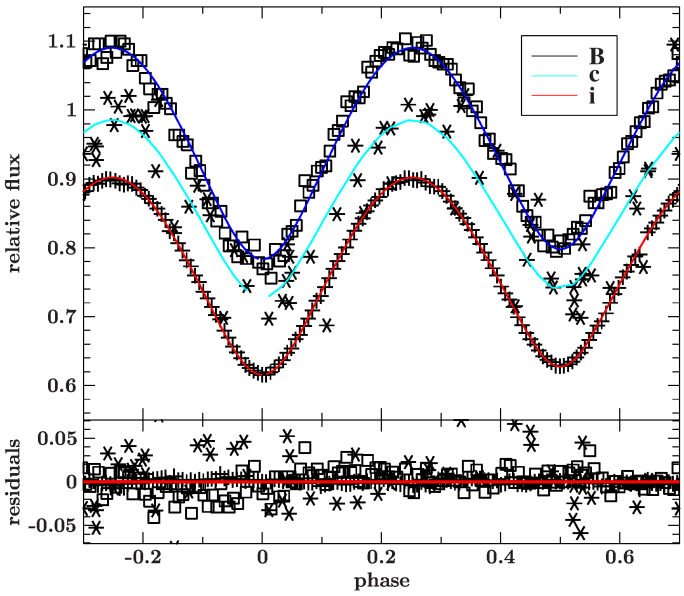

Fig. 5. Relative fluxes of the Johnson B-band (squares), ATLAS c-band (asterisks), and Sloan i-band (crosses) light curves compared to our best fit MORO models (blue, light-blue, and red, respectively). The light curves are shifted vertically for clarity. Residuals are shown at the bottom.

He II nebular lines. The difference to our previously reported values for the atmospheric parameters (Finch et al. 2018, 2019; Reindl et al. 2018) is a consequence of the rotational velocity which was neglected in our previous fits, as well as the extended model grid, the avoidance of observations which are noticeably affected by smearing of the lines due to the orbital motion of the system, the updated flux ratio of the system revealed by the light curve analysis, and the consideration of the DIB absorptions.

We emphasize that an accurate spectral analysis of the system is very challenging. This is because we lack the knowledge of the exact rotational velocities (the intrinsically broad He II lines are not a good approach to determine the rotational velocity, especially if only medium-resolution spectra are available), neglect the special geometry of the system, the incoming radiation of the other star, as well as metal opacities in our model atmosphere calculations. Finally the exact equivalent widths of the DIBs blending with He II λ 4686 Å and He II λ 5412 Å are not known, adding another uncertainty. The errors given in Table 2 therefore not only include the formal fitting errors, but also estimates on the systematic uncertainties mentioned above.

5. Light curve modelling

The analysis of the light curves was carried out simultaneously in the Johnson B-band, Sloan i-band, and ATLAS c-band filters. Because of its poor S/N, the ATLAS o-band light curve was omitted from our analysis. First fits of the light curves showed that the mass ratio is not constrained by the shape of the light curves. This is due to the significant degeneracies of the many dependent parameters used in the light curve analysis, which permits in many cases the determination of the mass ratio by light curve analysis (e.g., Schaffenroth et al. 2014). Only when ellipsoidal deformation is visible can the mass ratio be constrained (e.g., Kupfer et al. 2017). Therefore, we fixed the mass ratio of the system to the one which was derived by the RV analysis of He II λ 4542 Å and used the effective temperatures derived by the spectral analysis as starting values.

For the analysis we used MORO (Modified Roche Program, see Drechsel et al. 1995). It is based on the Wilson-Devinney mode 3 code, that is used for overcontact systems (see Kallrath & Milone 2009) using a modified Roche model considering the influence of the radiation pressure on the shape of the stars. The program assumes equal Roche potentials, limb darkening and gravitational darkening coefficients for both stars. The optimization of parameters is achieved by the simplex algorithm. The gravitational darkening parameters were fixed at 1.0 as predicted for radiative envelopes (von Zeipel 1924). The limb darkening coefficients were taken from Claret & Bloemen (2011) using the value closest to the parameters determined by the spectroscopic analysis for the different filters respectively. As both stars have comparable temperatures we also fixed the albedo to 1.0. We also considered a third light source, accounting for the nebular continuum and line emission. By varying the radiation pressure parameter, inclination, temperatures, Roche potentials, luminosity ratio of both stars, and the third light contribution, the curves are reproduced nicely. We note that our fit reproduces the light curves better than the one of García-Berro et al. (2016), and also slightly better than the model of SG+15.

Our best fits to the light curves are shown in Fig. 5 and the results of our analysis are summarized in Table 2 (see also Table B.1 for all parameters of the best light curve fit). We find a relative luminosity $\frac{L_1}{L_1+L_2}$ of 58.37% in the B-band, similar effective temperatures for both stars ($T_{\rm eff} \approx 40$ kK), and that the mean radius of the secondary is 15% smaller than the radius of the primary. We derived an additional constant flux component of 0.8% in B, 2.8% in i, and 20.5% in the ATLAS c-band[6]. Combining it

[6] We note, that for compact nebulae, the flux contribution of the nebular lines can be significant when broad band filters are used (Shaw & Kaler 1985; Gathier & Pottasch 1988). For example the V-band magnitude of the CSPN of the Stingray Nebula measured with the *Hubble* Space Telescope and, thus, resolving the CSPN, is four orders of magnitude smaller than what is measured from the ground (Bobrowsky et al. 1998; Schaefer & Edwards 2015). Therefore, the high additional flux contributions in the ATLAS c-band, which covers numerous nebular lines (e.g., [O III] λ 5007 Å), is not surprising.

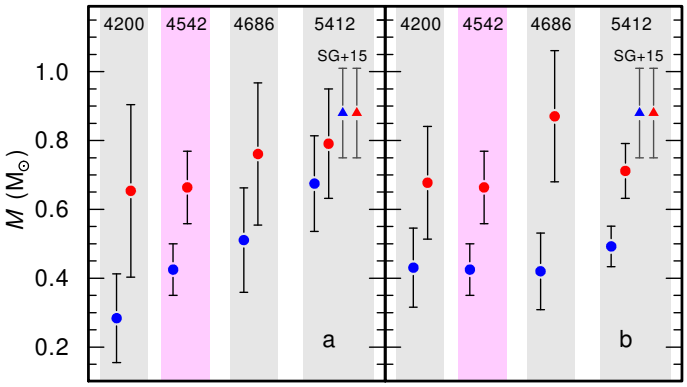

Fig. 6. Dynamical masses of the primary (red dots) and the secondary (blue dots) as determined with the inclination angle from our light curve analysis and our RV fitting of the four He II lines excluding (*panel a*) and including DIBs (*panel b*). Masses obtained from He II lines that blend with DIBs are highlighted in grey, He II λ 4542 Å which is not blended with any DIB is highlighted in pink. The blue and red triangles are the masses reported by SG+15.

with the results from the RV curves the absolute parameters M, R could be derived (Table 2, see also Sect. 6). The errors were determined by a bootstraping method (see Schaffenroth et al. 2014) and represent only the statistical error resulting from the noise in the light curves and do not consider the degeneracies in the light curve.

6. Dynamical masses and evolutionary status

Since the inclination of the system (i = 63.59 ± 0.54°) can be constrained well from the light curve fitting, the dynamical masses of the two stars can be calculated via the binary mass function

$$f(M_1, M_2) = \frac{K_1^3 P}{2\pi G} = \frac{M_2 \sin^3 i}{\left(1 + \frac{M_1}{M_2}\right)^2}.$$

Our results are shown in Fig. 6. In panel a, we show the dynamical masses as obtained using our Voigt profile fitting routine and neglecting DIBs. It can be seen, that our masses obtained from He II λ 5412 Å with the Voigt profile RV fitting and after applying the zero point correction (M_1 = 0.79 ± 0.16 $M_\odot$ and M_2 = 0.67 ± 0.14 $M_\odot$) agree within the error limits with the results of SG+15, who find 0.88 ± 0.13 $M_\odot$ for both stars. However, for all other lines contradictory results are found.

When DIBs are included in the RV fitting significantly different results are obtained for the masses of the two CSPNe (e.g., M_1 = 0.71 ± 0.08 $M_\odot$ and M_2 = 0.49 ± 0.06 $M_\odot$ for He II λ 5412 Å, panel b in Fig. 6). In this case we find that the masses from the different He II lines agree with each other, but no longer with the results from SG+15. This is a consequence of the zeropoint corrections, using Voigt profiles instead of Gaussians in the RV fitting, and most importantly the inclusion of DIBs when determining the RVs.

We stress that masses obtained from He II $\lambda\lambda$ 4200, 4542 Å are the ones to be trusted. This is because only He II λ 4542 Å is not blended with any DIB and for He II λ 4200 Å a good fit to the DIB which blends with this line can be found, though the S/N in this part of the spectrum is rather poor. For He II λ 4686 Å and He II λ 5412 Å we can only assume the DIBs are of about the same strength as in HD 204827 based on the similar reddening. However, the equivalent widths of the DIBs blending with these lines might be different, for example because of a different chemical composition of the interstellar or circumstellar medium.

The masses obtained for He II λ 4542 Å are M_1 = 0.66 ± 0.11 $M_\odot$ and M_2 = 0.42 ± 0.07 $M_\odot$, and agree very well with the masses obtained from He II λ 4200 Å (M_1 = 0.68 ± 0.16 $M_\odot$ and M_2 = 0.43 ± 0.11 $M_\odot$). This is a striking result, as with the masses derived from He II λ 4542 Å the total mass of the system (M = 1.08 ± 0.18), no longer exceeds the Chandrasekhar mass limit.

The total mass of the system is still high enough that a merger of the system will occur within a Hubble time. However, with the combined dynamical mass of the system no longer exceeding the Chandrasekhar mass limit, the merger will not produce a SN Ia via the traditional double-degenerate channel (Han & Podsiadlowski 2004). The individual masses of the two CSPNe are also too small for a reasonable production of 56Ni (which determines the explosion brightness) in case of a dynamical explosion during the merger process (Pakmor et al. 2013; Shen et al. 2018). Thus, the merging event of Hen 2−428 will not be identified as a SN Ia.

Most likely, the merger of Hen 2−428 will then lead to the formation of a (He-rich) RCB star → EHe star → massive O(He) star → CO white dwarf (Schwab 2019; Shen 2015; Zhang et al. 2014). If both stars should have CO-cores at the time of the merger, the formation of a star with a C/O-dominated atmosphere could be possible. This would make Hen 2−428 a promising progenitor for the CO-dominated hot white dwarf stars H1504+65 and RXJ0439.8−6809 (Werner & Rauch 2015), and for the C-dominated hot DQ white dwarfs (Kawka et al. 2020). The formation of an AM CVn type system via the double white dwarf channel (Paczyński 1967), that will end up in a faint thermonuclear supernova, however, seems very unlikely due to the high mass ratio of the system (Nelemans et al. 2001; Marsh et al. 2004).

In Fig. 7, we show the locations of the two CSPNe in the Hertzsprung Russell diagram (HRD), as derived with the effective temperatures from our spectroscopic analysis and the radii from the light curve analysis (primary is shown in red, the secondary in blue). It can be seen, that the luminosities and radii of the two stars are too low for what is expected for normal post-asymptotic giant branch (AGB) stars (black lines indicate H-shell burning post-AGB tracks from Miller Bertolami 2016). The dynamical mass and location in the HRD of the secondary agrees with predications for post-RGB stars (light-blue lines, Hall et al. 2013), while the dynamical mass of the primary is too high for this scenario. The secondary could also be a post-extreme horizontal branch (post-EHB) star (pink lines in Fig. 7 are post-EHB tracks from Dorman et al. 1993), while the mass of the primary is again too high for this scenario. It is worthwhile mentioning that the mass of the remaining H layer (≤0.001 $M_\odot$) of EHB stars is much too low to produce a nebula at the end of the He-core burning stage. Thus, it is not possible for both stars to be post-EHB stars.

The solid purple lines in Fig. 7 correspond to evolutionary tracks for stars stripped through Roche-lobe overflow and were calculated by Götberg et al. (2018). The stars had initial masses of 3.65, 2.99, and 2.44 $M_\odot$ and the tracks show the evolution from central H-burning, the mass transfer phase, consequent blue-ward evolution, until He-core burning is reached. The mass of the secondary is too small in order to descend from such a star, while the primary could be a candidate for being a stripped He-star, shortly before the central He-core burning phase. The surface He abundances predicted by Götberg et al. (2018) for this evolutionary stage ($X_{\rm He} \approx -0.15$) matches surprisingly well

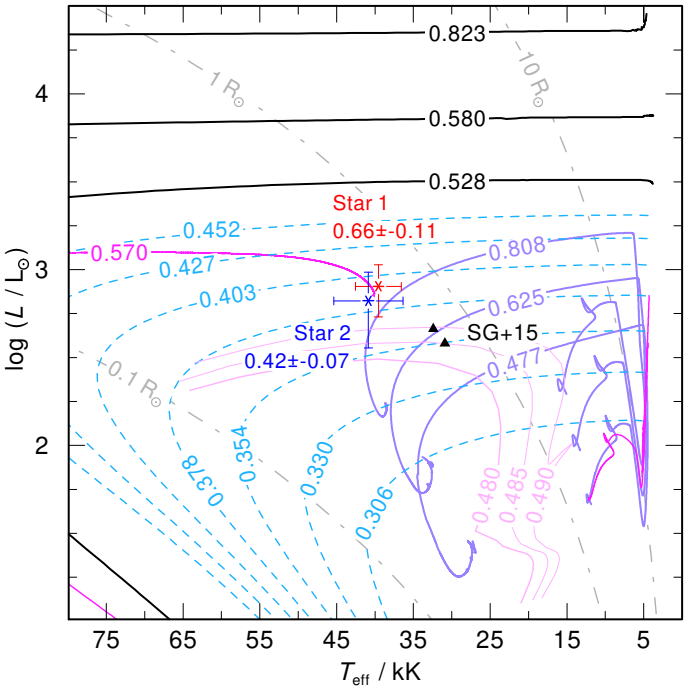

Fig. 7. Locations of the two CSPNe and their dynamical masses (primary is shown in red, the secondary in blue) in the HRD compared to stellar evolutionary tracks. Black lines indicate H-shell burning post-AGB tracks from Miller Bertolami (2016), dashed, light-blue lines post-RGB tracks from Hall et al. (2013), purple lines stripped star evolutionary tracks from Götberg et al. (2018), and in pink post-EHB evolutionary tracks from Dorman et al. (1993). The magenta line indicates an evolutionary track of a He-shell burning stripped post-early AGB star. The gray dashed-dotted lines indicate radii of 0.1, 1, and 10 $R_\odot$.

with what we find in our spectroscopic analysis of the primary ($X_{\rm He} = -0.16$).

We stress that the comparison with these evolutionary tracks should be treated with caution, as obviously none of these models can account for the real evolution of Hen 2−428. Stable Roche-lobe overflow, for example, cannot account for the short orbital period and over-contact nature of the system, meaning the latest mass-transfer phase must have ended in a common envelope ejection. In addition it is not clear to what extent the evolutionary tracks (and the mass-radius relationship) are altered for over-contact systems. Short orbital period ($P < 1$ d) low-mass main sequence stars, for example, show an inflation by 10% (Kraus et al. 2011), thus it could be possible that the radii and luminosities of two CSPNe of Hen 2−428 are also too large compared to single-star evolutionary tracks. For the massive over-contact system VFTS 352 (temperature-wise very similar to Hen 2−428), it was found that single-star models predict effective temperatures which are 6% lower than what would be expected from the dynamical masses (Almeida et al. 2015).

With all caveats in mind we can still make an educated guess of what the evolution of the system might have been. In light of the actual close configuration of the system and the presence of surrounding material we know that the last mass transfer episode was unstable and led to the formation and ejection of a common envelope. In addition, the derived dynamical masses ($M_1 = 0.66 \pm 0.11\,M_\odot$ and $M_2 = 0.42 \pm 0.07\,M_\odot$), temperatures and luminosities (and radii), together with a comparison with stellar evolution models suggests that the secondary (in the following Star 2) has a post-RGB like structure, meaning it has a degenerate He-core surrounded by a H-burning shell and a thin envelope on top. The nature of the more massive component (in the following Star 1) is less certain. The actual mass of the object, however, indicates that before the last mass transfer episode Star 1 was not a low-mass RGB star and its mass before the last mass transfer episode was beyond that needed for non-degenerate He ignition. As Star 2 is already a low-mass evolved star we can safely conclude that Star 1 was originally the less massive component and increased its mass during a previous (first) mass transfer episode. This implies that the total initial mass of the system was necessarily $M_1^i + M_2^i \lesssim 3.6\,M_\odot$ (Bressan et al. 2012), and $M_2 \lesssim 3.2\,M_\odot$ before the common envelope episode.

As mentioned above, the inferred surface properties and mass of Star 1 are in good agreement with the predicted evolution of a intermediate mass star that was stripped of in its post-main sequence evolution before the ignition of He-core burning. A serious shortcoming of this scenario is that, for this to happen, Star 1 needs to fill its Roche lobe before He-ignition, but intermediate-mass stars with $M_2 \approx 3.2\,M_\odot$ reach at most $R_2 \sim 45\,R_\odot$ before He-ignition. With a q-value of $q \approx 3.2\,M_\odot/0.4\,M_\odot = 8$ that means that the Roche lobe of the $0.4\,M_\odot$ companion should have been $R_1 \lesssim 18\,R_\odot$ at the end of the first (stable) mass transfer episode. Due to the tight core mass-radius relation of RGB stars, and the fact that during Roche lobe overflow $R_\star \simeq R_{\rm Roche}$ (Han et al. 2000), Star 2 would have probably been peeled off well before the mass of the degenerate He-core reached $\approx 0.3\,M_\odot$. Given that $M_2 = 0.42 \pm 0.07\,M_\odot$, this scenario seems unlikely.

Interestingly, stars with masses in the range $2.5{-}3\,M_\odot$ expand in the early-AGB phase[7] to very large radii of $R_\star > 100\,R_\odot$. Moreover, during the early AGB, a star in this mass range shuts down its H-burning shell, making the stripping of the H-rich material easier, which in the light of the high He enrichment found in the primary of the system makes this scenario more compeling. The magenta line in Fig. 7 shows the evolution of a $0.57\,M_\odot$ post-early AGB model constructed by artificially stripping the envelope of a $2.5\,M_\odot$ star once it reached the luminosity of Star 1. The surface He mass fraction of the model is $X_{\rm He} \approx -0.28$.

Figure 8 shows a toy model for such scenario. Lets assume that we start the evolution with a pair of low-mass stars in a relatively close orbit (panel A in Fig. 8, $M_2^i = 1.55\,M_\odot$, $M_1^i = 1.3\,M_\odot$, $a \simeq 33\,R_\odot$). As soon as the more massive star ends its main sequence evolution it will evolve into the RGB and when it reaches $R_1 \simeq 13\,R_\odot$ it will start to transfer mass to its companion (panel B in Fig. 8). Due to the low mass ratio of the system at that point ($q \lesssim 1.19$) mass transfer will be stable, and as soon as $M_1 < M_2$ it will evolve on a nuclear timescale (Podsiadlowski 2014), and stable mass transfer continues as Star 2 evolves on the RGB. If the envelope of Star 2 is removed once its He-degenerate core reaches $0.35\,M_\odot$ the star will contract and form a $M_2^f \simeq 0.35\,M_\odot$ He-core white dwarf. Under the simplifying assumption that mass loss is conservative (Postnov & Yungelson 2014) our system would be composed of a $0.35\,M_\odot$ He-core white dwarf, and a rejuvenated $M_1^{\rm rj} = 2.5\,M_\odot$ main-sequence companion, separated by $a \simeq 174\,R_\odot$. The Roche lobe of Star 1 under such situation would be of $R_{\rm Roche}^1 \simeq 95\,R_\odot$[8].

[7] This is, after the end of core-helium burning and before the development of thermal pulses.

[8] We note however that this is just a toy model, as the sequence in Fig. 7 was stripped on the AGB at $R \simeq 50\,R_\odot$ in order to match the luminosity of the primary component.

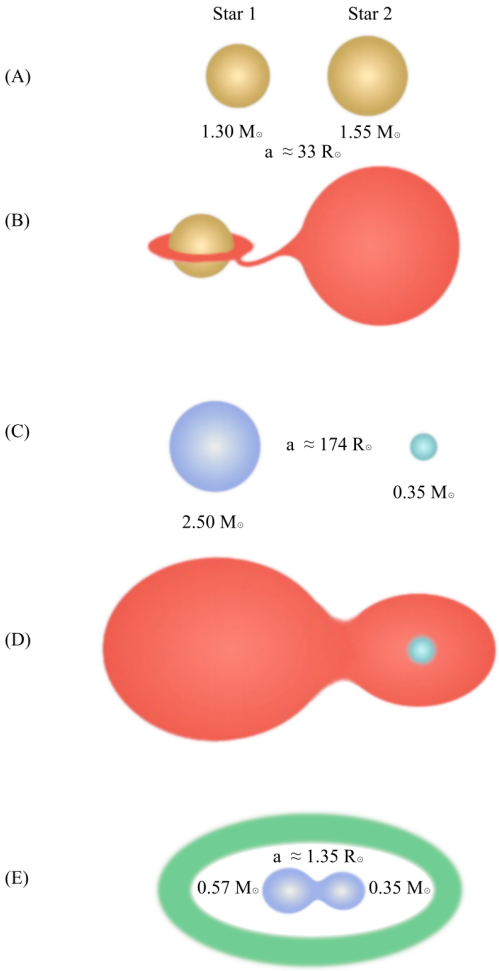

Fig. 8. Sketch of a possible evolutionary scenario for Hen 2−428.

Star 1 will then end its main sequence phase, and go to the He-core burning phase without interacting with its companion. But once He-core burning is finished, the star will evolve to the early AGB. In isolation a 2.5 $M_{\odot}$ star would expand to about $R^1 \approx 170\,R_{\odot}$ before developing thermal pulses, but due to the presence of its companion as soon as Star 1 fills its Roche lobe at $R^1_{\rm Roche} \simeq 95\,R_{\odot}$ it will start transferring mass. Given the extreme mass ratio of the system ($q = M^{\rm ri}_1/M^f_2 \simeq 7.14$) mass transfer will be highly unstable, leading to the formation of a common envelope (panel D in Fig. 8), the shrinking of the orbits and the final ejection of the common envelope. The current state of the system would be an overcontact close binary system composed of the post-early AGB core of $M^f_1 \simeq 0.57\,M_{\odot}$, a post-RGB core of $M^f_2 \simeq 0.35\,M_{\odot}$ with its envelope reheated by the last mass transfer episode, and a surrounding PN composed of the ejected material (panel E in Fig. 8).

7. Summary and conclusion

We performed a detailed reanalysis of the alleged type Ia supernova progenitor Hen 2−428. Our study reveals that the red-excess reported by Rodríguez et al. (2001) is merely a consequence of the Cardelli et al. (1989) reddening law used in their work. Fitting the IDS spectrum with our best fit model and using the Fitzpatrick (1999) reddening law we find $A_V = 3.57 \pm 0.16$ mag, which is slightly higher than the value ($A_V = 2.96 \pm 0.34$ mag) reported by Rodríguez et al. (2001).

Furthermore, we discovered zeropoint shifts in the wavelengths calibration of the OSIRIS spectra up to 54 km s^{-1} (Table 1). Correcting for these and using Voigt profiles instead of Gaussian profiles in the RV fitting, our results for He II λ 5412 Å agree with the values reported by SG+15, but for all other He II lines we end up with conflicting RV amplitudes.

This issue was resolved by the realization that the spectra, and most notably three of the four double-lined He II lines, are contaminated by DIBs. Including the DIBs in the RV fitting, we obtain consistent results for all four He II lines and importantly, very distinct RV amplitudes of $K_1 = 137 \pm 12$ km s^{-1} for the primary and $K_2 = 214 \pm 14$ km s^{-1} for the secondary (using He II λ 4542 Å, the only line not blended with any DIB). These values no longer agree with the results of SG+15.

We then performed spectroscopic fits to the He II lines using metal-free non-LTE models. Using the results from the RV and spectral analysis, we carried out light curve fits to the *B*-band, Sloan *i*-band, and ATLAS *c*-band filters, to derive the geometry of the system. We find the effective temperatures of both stars are about the same ($T_{\rm eff} \approx 40$ kK), but higher than reported by SG+15. The radii of the two stars (0.603 $R_{\odot}$ for the primary and 0.514 $R_{\odot}$ for the secondary) are also found to differ from the results of SG+15, who found $R = 0.68\,R_{\odot}$ for both stars. The inclination angle found by us ($i = 63.59 \pm 0.54°$) agrees within the error limits with what is reported by SG+15 ($i = 64.7 \pm 1.4°$).

The most striking result of our analysis is that the mass ratio of the system no longer equals one and that the dynamical masses of both stars ($M_1 = 0.66 \pm 0.11\,M_{\odot}$ and $M_2 = 0.42 \pm 0.07\,M_{\odot}$) are significantly smaller compared to the results of SG+15 ($M_1 = M_2 = 0.88 \pm 0.13\,M_{\odot}$). The total mass of the system ($M = 1.08 \pm 0.18$) no longer exceeds the Chandrasekhar mass limit, which again, is mainly a result of blends of He II λ 5412 Å with DIBs, which have led to an overestimation of the dynamical masses of Hen 2−428 by SG+15. With these new findings, the merging event of Hen 2−428 will not be recognised as SN Ia, but most likely lead to the formation of a H-deficient star.

Based on the dynamical masses and atmospheric parameters revealed by our work, we propose that the primary is a He-shell burning post-early AGB star, and the secondary is the reheated core of a post-RGB star. The formation of the system could be explained by a first stable mass transfer epsiode in which Star 2 (now secondary) tranfered most of its mass to Star 1 (now primary) before it ignited He-core burning. As Star 1 evolved up the early AGB, a common envelope was formed, and later ejected, with the ejected material being now visible as the PN.

Even though the system can no longer be considered as a SN Ia progenitor, this does not diminish the importance of Hen 2−428 for studying common envelope evolution, the formation of H-deficient stars via the double white dwarf merger channel, and the creation of (asymmetrical) PNe via non-canonical (i.e., non-post-AGB) evolutionary path ways. Hen 2−428 is the only double-degenerate CSPN observed in an over-contact configuration, thus, it might provide insights on the common envelope ejection efficiency. Future spectroscopic observations offering a better S/N especially in the blue part of the spectrum could improve the dynamical masses and help to better constrain the evolutionary status of this interesting system. A nebular abundance analysis will help to determine the metallicity of the system. Finally, detailed evolutionary calculations that are able to reproduce the history and future evolution of the system are highly encouraged.

Acknowledgements. We thank Mónica Rodríguez for providing us with the INT/IDS spectra. We appreciate useful discussions with David Jones and Tom Marsh during the CWDB meeting. V.S. is supported by the Deutsche Forschungsgemeinschaft, DFG through grant GE 2506/9-1. Part of this work was supported by a MinCyT-DAAD bilateral cooperation program through grant DA/16/07. Based on data from the GTC PublicArchive at CAB (INTA-CSIC). Based on observations collected at the European Organisation for Astronomical Research in the Southern Hemisphere under ESO programme 295.D-5032(A). IRAF is distributed by the National Optical Astronomy Observatory, which is operated by the Association of Universities for Research in Astronomy (AURA) under a cooperative agreement with the National Science Foundation. This work includes data from the Asteroid Terrestrial-impact Last Alert System (ATLAS) project. ATLAS is primarily funded to search for near earth asteroids through NASA grants NN12AR55G, 80NSSC18K0284, and 80NSSC18K1575; by products of the NEO search include images and catalogs from the survey area. The ATLAS science products have been made possible through the contributions of the University of Hawaii Institute for Astronomy, the Queen's University Belfast, the Space Telescope Science Institute, and the South African Astronomical Observatory.

References

Almeida, L. A., Sana, H., de Mink, S. E., et al. 2015, ApJ, 812, 102
Arkhipova, V. P., Ikonnikova, N. P., Kniazev, A. Y., & Rajoelimanana, A. 2013, Astron. Lett., 39, 201
Asplund, M., Grevesse, N., Sauval, A. J., & Scott, P. 2009, ARA&A, 47, 481
Barnard, A. J., Cooper, J., & Shamey, L. J. 1969, A&A, 1, 28
Barnard, A. J., Cooper, J., & Smith, E. W. 1974, J. Quant. Spectr. Radiat. Transf., 14, 1025
Bloecker, T. 1993, Acta Astron., 43, 305
Bloecker, T., & Schoenberner, D. 1991, A&A, 244, L43
Bobrowsky, M., Sahu, K. C., Parthasarathy, M., & García-Lario, P. 1998, Nature, 392, 469
Breedt, E., Steeghs, D., Marsh, T. R., et al. 2017, MNRAS, 468, 2910
Bressan, A., Marigo, P., Girardi, L., et al. 2012, MNRAS, 427, 127
Burdge, K. B., Coughlin, M. W., Fuller, J., et al. 2019, Nature, 571, 528
Campbell, E. K., Holz, M., Gerlich, D., & Maier, J. P. 2015, Nature, 523, 322
Cardelli, J. A., Clayton, G. C., & Mathis, J. S. 1989, ApJ, 345, 245
Claret, A., & Bloemen, S. 2011, A&A, 529, A75
Corradi, R. L. M., García-Rojas, J., Jones, D., & Rodríguez-Gil, P. 2015, ApJ, 803, 99
Davignon, G., Blecha, A., Burki, G., et al. 2004, in CCD Camera and Automatic Data Reduction Pipeline for the Mercator Telescope on La Palma, eds. A. F. M. Moorwood, & M. Iye, SPIE Conf. Ser., 5492, 871
De Marco, O., Farihi, J., & Nordhaus, J. 2009, J. Phys. Conf. Ser., 172, 012031
Dorman, B., Rood, R. T., & O'Connell, R. W. 1993, ApJ, 419, 596
Drechsel, H., Haas, S., Lorenz, R., & Gayler, S. 1995, A&A, 294, 723
Fink, M., Hillebrandt, W., & Röpke, F. K. 2007, A&A, 476, 1133
Fink, M., Röpke, F. K., Hillebrandt, W., et al. 2010, A&A, 514, A53
Finch, N. L., Reindl, N., Barstow, M. A., et al. 2018, Open Astron., 27, 57
Finch, N. L., Braker, I. P., Reindl, N., et al. 2019, in Spectral Analysis of Binary Pre-white Dwarf Systems, eds. K. Werner, C. Stehle, T. Rauch, & T. Lanz, ASP Conf. Ser., 519, 231
Fitzpatrick, E. L. 1999, PASP, 111, 63
Frew, D. J., Parker, Q. A., & Bojičić, I. S. 2016, MNRAS, 455, 1459
García-Berro, E., Soker, N., Althaus, L. G., Ribas, I., & Morales, J. C. 2016, New Astron., 45, 7
Gathier, R., & Pottasch, S. R. 1988, A&A, 197, 266
Geier, S., Hirsch, H., Tillich, A., et al. 2011, A&A, 530, A28
Götberg, Y., de Mink, S. E., Groh, J. H., et al. 2018, A&A, 615, A78
Griem, H. R. 1974, in Spectral Line Broadening by Plasmas (New York: Academic Press, Inc.), Pure Appl. Phys., 39, 421
Gvaramadze, V. V., Gräfener, G., Langer, N., et al. 2019, Nature, 569, 684
Hall, P. D., Tout, C. A., Izzard, R. G., & Keller, D. 2013, MNRAS, 435, 2048
Han, Z., & Podsiadlowski, P. 2004, MNRAS, 350, 1301
Han, Z., Tout, C. A., & Eggleton, P. P. 2000, MNRAS, 319, 215
Henize, K. G. 1976, ApJS, 30, 491
Hillwig, T. C., Frew, D. J., Reindl, N., et al. 2017, AJ, 153, 24
Hirsch, H. A. 2009, PhD Thesis, University Erlangen-Nürnberg, Germany
Hobbs, L. M., York, D. G., Snow, T. P., et al. 2008, ApJ, 680, 1256
Iben, I., Jr., & Tutukov, A. V. 1984, ApJS, 54, 335
Iben, I., Jr., & Tutukov, A. V. 1986, ApJ, 311, 742
Jenniskens, P., & Desert, F.-X. 1994, A&AS, 106, 39
Jones, D. 2019, in Highlights on Spanish Astrophysics X, eds. B. Montesinos, A. Asensio Ramos, F. Buitrago, et al., 340
Jones, D. 2020, ArXiv e-prints [arXiv:2001.03337]
Jones, E., Oliphant, T., Peterson, P., et al. 2001, SciPy: Open Source Scientific Tools for Python
Justham, S., Podsiadlowski, P., & Han, Z. 2011, MNRAS, 410, 984
Kallrath, J., & Milone, E. F. 2009, Eclipsing Binary Stars: Modeling and Analysis (New York: Springer-Verlag)
Kashi, A., & Soker, N. 2011, MNRAS, 417, 1466
Kawka, A., Vennes, S., & Ferrario, L. 2020, MNRAS, 491, L40
Kos, J., & Zwitter, T. 2013, ApJ, 774, 72
Kraus, A. L., Tucker, R. A., Thompson, M. I., Craine, E. R., & Hillenbrand, L. A. 2011, ApJ, 728, 48
Krełowski, J., Galazutdinov, G., Godunova, V., & Bondar, A. 2019, Acta Astron., 69, 159
Kupfer, T., van Roestel, J., Brooks, J., et al. 2017, ApJ, 835, 131
Lallement, R., Capitanio, L., Ruiz-Dern, L., et al. 2018, A&A, 616, A132
Liu, D. D., Wang, B., Podsiadlowski, P., & Han, Z. 2016, MNRAS, 461, 3653
Liu, D., Wang, B., & Han, Z. 2018, MNRAS, 473, 5352
Maoz, D., Mannucci, F., & Nelemans, G. 2014, ARA&A, 52, 107
Marsh, T. R., Nelemans, G., & Steeghs, D. 2004, MNRAS, 350, 113
Miller Bertolami, M. M. 2016, A&A, 588, A25
Napiwotzki, R. 1999, A&A, 350, 101
Napiwotzki, R., Christlieb, N., Drechsel, H., et al. 2001, Astron. Nachr., 322, 411
Napiwotzki, R., Karl, C. A., Lisker, T., et al. 2020, A&A, in press, https://doi.org/10.1051/0004-6361/201629648
Nelemans, G., Portegies Zwart, S. F., Verbunt, F., & Yungelson, L. R. 2001, A&A, 368, 939
Paczyński, B. 1967, Acta Astron., 17, 287
Paczynski, B. 1976, in Structure and Evolution of Close Binary Systems, eds. P. Eggleton, S. Mitton, & J. Whelan, IAU Symp., 73, 75
Pakmor, R., Hachinger, S., Röpke, F. K., & Hillebrandt, W. 2011, A&A, 528, A117
Pakmor, R., Kromer, M., Taubenberger, S., & Springel, V. 2013, ApJ, 770, L8
Podsiadlowski, P. 2014, Binary Systems, their Evolution and Environments, 13
Postnov, K. A., & Yungelson, L. R. 2014, Liv. Rev. Relativ., 17, 3
Rauch, T., & Deetjen, J. L. 2003, in Stellar Atmosphere Modeling, eds. I. Hubeny, D. Mihalas, & K. Werner, ASP Conf. Ser., 288, 103
Rebassa-Mansergas, A., Toonen, S., Korol, V., & Torres, S. 2019, MNRAS, 482, 3656
Reindl, N., Rauch, T., Werner, K., Kruk, J. W., & Todt, H. 2014a, A&A, 566, A116
Reindl, N., Rauch, T., Parthasarathy, M., et al. 2014b, A&A, 565, A40
Reindl, N., Finch, N., Schaffenroth, V., et al. 2018, Galaxies, 6, 88
Renedo, I., Althaus, L. G., Miller Bertolami, M. M., et al. 2010, ApJ, 717, 183
Rodríguez, M., Corradi, R. L. M., & Mampaso, A. 2001, A&A, 377, 1042
Saio, H., & Jeffery, C. S. 2002, MNRAS, 333, 121
Santander-García, M., Rodríguez-Gil, P., Corradi, R. L. M., et al. 2015, Nature, 519, 63
Schaefer, B. E., & Edwards, Z. I. 2015, ApJ, 812, 133
Schaffenroth, V., Geier, S., Heber, U., et al. 2014, A&A, 564, A98
Schlafly, E. F., Finkbeiner, D. P., Schlegel, D. J., et al. 2010, ApJ, 725, 1175
Schöning, T., & Butler, K. 1989, A&AS, 78, 51
Schwab, J. 2019, ApJ, 885, 27
Shaw, R. A., & Kaler, J. B. 1985, ApJ, 295, 537
Shen, K. J. 2015, ApJ, 805, L6
Shen, K. J., Kasen, D., Miles, B. J., & Townsley, D. M. 2018, ApJ, 854, 52
Sparks, W. M., & Stecher, T. P. 1974, ApJ, 188, 149
Tonry, J. L., Denneau, L., Heinze, A. N., et al. 2018, PASP, 130, 064505
Tremblay, P.-E., & Bergeron, P. 2009, ApJ, 696, 1755
Tylenda, R., Stasińska, G., Acker, A., & Stenholm, B. 1994, A&AS, 106, 559
van Hoof, P. A. M. 2018, Galaxies, 6, 63
von Zeipel, H. 1924, MNRAS, 84, 665
Webbink, R. F. 1984, ApJ, 277, 355
Weisberg, J. M., & Taylor, J. H. 2005, in The Relativistic Binary Pulsar B1913+16: Thirty Years of Observations and Analysis, eds. F. A. Rasio, & I. H. Stairs, ASP Conf. Ser., 328, 25
Werner, K., & Rauch, T. 2015, A&A, 584, A19
Werner, K., Deetjen, J. L., Dreizler, S., et al. 2003, in Stellar Atmosphere Modeling, eds. I. Hubeny, D. Mihalas, & K. Werner, ASP Conf. Ser., 288, 31
Werner, K., Dreizler, S., & Rauch, T. 2012, Astrophysics Source Code Library [record ascl:1212.015]
Woosley, S. E., & Weaver, T. A. 1994, ApJ, 423, 371
Zhang, X., & Jeffery, C. S. 2012a, MNRAS, 419, 452
Zhang, X., & Jeffery, C. S. 2012b, MNRAS, 426, L81
Zhang, Y., Fang, X., Chau, W., et al. 2012, ApJ, 754, 28
Zhang, X., Jeffery, C. S., Chen, X., & Han, Z. 2014, MNRAS, 445, 660

Appendix A: Additional figure

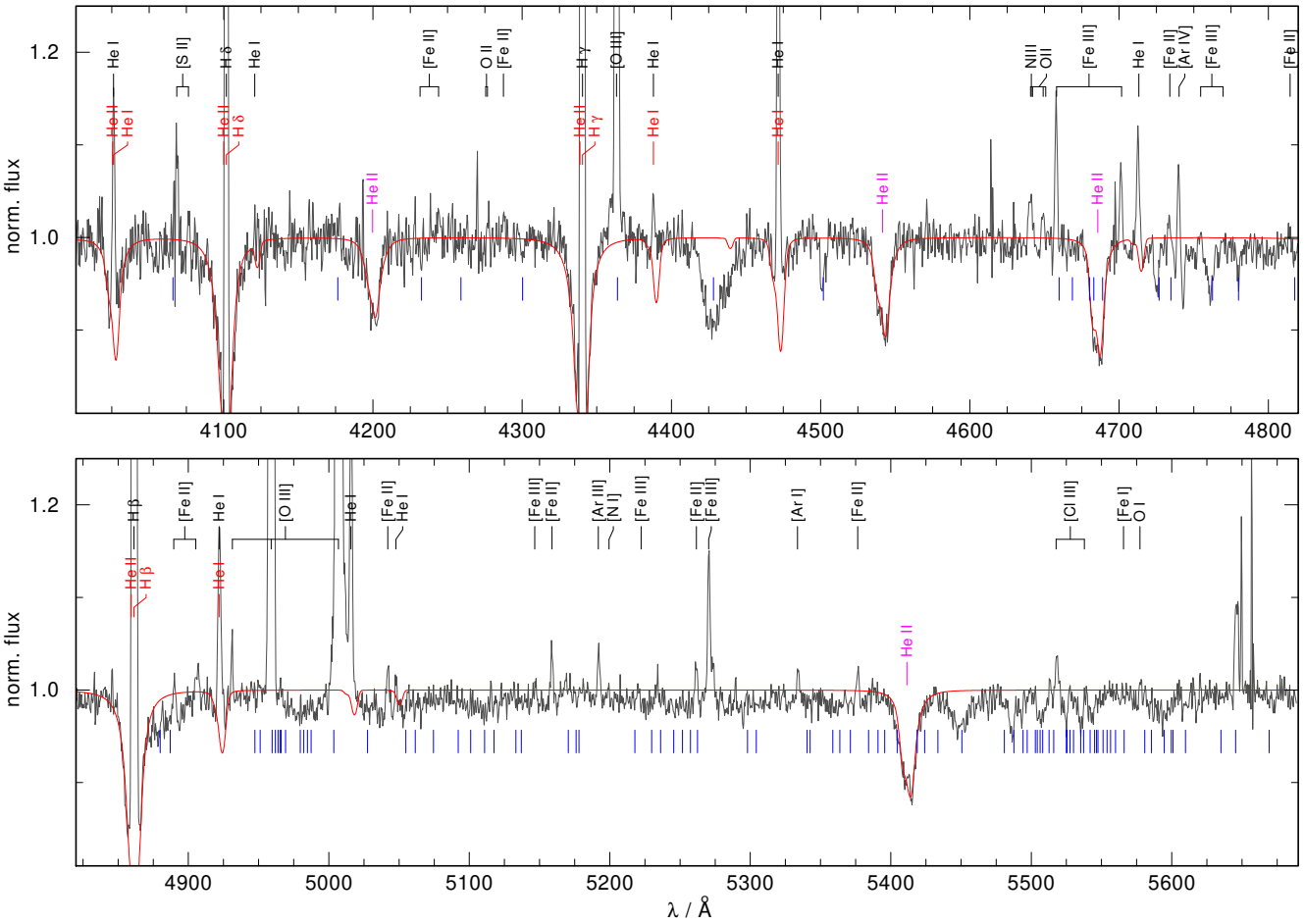

Fig. A.1. Normalized OSIRIS observation #2 (gray) compared to our best fit TMAP model (red). The locations of known diffuse interstellar bands (blue), nebular (black), and photospheric lines (red) are marked. Photospheric lines used in for the RV analysis are marked in magenta.

Appendix B: Additional table

Table B.1. Best light curve solution of Hen 2−428.

Fixed parameters:		
$q\,(=M_2/M_1)$		0.64
A_1 [(a)]		1.0
A_2 [(a)]		1.0
g_1 [(b)]		1.0
g_2 [(b)]		1.0
$x_1(B)$ [(c)]		0.25
$x_1(i)$ [(c)]		0.17
$x_1(c)$ [(c)]		0.20
$x_2(B)$ [(c)]		0.25
$x_2(i)$ [(c)]		0.17
$x_2(c)$ [(c)]		0.20
Adjusted parameters:		
i	[°]	63.59 ± 0.54
$T_{\rm eff}(1)$	[K]	40179 ± 370
$T_{\rm eff}(2)$	[K]	40356 ± 175
δ_1 [(d)]		0.02174 ± 0.0052
δ_2 [(d)]		0.0033 ± 0.0021
$\frac{L_1}{L_1+L_2}(B)$ [(e)]		0.5837 ± 0.0068
$\frac{L_1}{L_1+L_2}(i)$ [(e)]		0.5842 ± 0.0068
$\frac{L_1}{L_1+L_2}(c)$ [(e)]		0.5939 ± 0.0168
Ω_1 [(f)]		2.965 ± 0.017
Ω_2 [(f)]		2.965 ± 0.017
$l_3(B)$ [(g)]		0.0079 ± 0.0043
$l_3(i)$ [(g)]		0.0279 ± 0.0066
$l_3(c)$ [(g)]		0.2046 ± 0.0312
Roche radii [(h)]:		
r_1(mean)	[a]	0.4472 ± 0.0041
r_1(pole)	[a]	0.4121 ± 0.0030
r_1(point)	[a]	−1.0000
r_1(side)	[a]	0.4407 ± 0.0039
r_1(back)	[a]	0.4806 ± 0.0056
r_2(mean)	[a]	0.3809 ± 0.0042
r_2(pole)	[a]	0.3465 ± 0.0028
r_2(point)	[a]	−1.0000
r_2(side)	[a]	0.3676 ± 0.0036
r_2(back)	[a]	0.4212 ± 0.0067

Notes. [(a)]Bolometric albedo. [(b)]Gravitational darkening exponent. [(c)]Linear limb darkening coefficient; taken from Claret & Bloemen (2011). [(d)]Radiation pressure parameter, see Drechsel et al. (1995). [(e)]Relative luminosity; L_2 is not independently adjusted, but recomputed from r_2 and $T_{\rm eff}(2)$.[(f)]Roche potentials. [(g)]Fraction of third light at maximum. [(h)]Fractional Roche radii in units of separation of mass centers.